Extending the depth of focus of fiber-optic optical coherence tomography using a chromatic dual-focus design

JINHAN LI,[1] YUEMEI LUO,[1] XIANGHONG WANG,[1] NANSHUO WANG,[1] EN BO,[1] SI CHEN,[1] SHUFEN CHEN,[1] SHI CHEN,[1] MENG-TSAN TSAI[3,4], AND LINBO LIU[1,2,*]

[1]*School of Electrical and Electronic Engineering, Nanyang Technological University, Singapore 639798*
[2]*School of Chemical and Biomedical Engineering, Nanyang Technological University, Singapore 637459*
[3]*Department of Electrical Engineering, Chang Gung University, Taoyuan 33302, Taiwan*
[4]*Department of Dermatology, Chang Gung Memorial Hospital, Linkou 33305, Taiwan*
**Corresponding author: LIULINBO@ntu.edu.sg*

Received XX Month XXXX; revised XX Month, XXXX; accepted XX Month XXXX; posted XX Month XXXX (Doc. ID XXXXX); published XX Month XXXX

We report a dual-focus fiber-optic probe designed to extend depth-of-focus (DOF) in high-resolution endoscopic optical coherence tomography (OCT). We exploited the broad spectral bandwidth of a supercontinuum source and, in the fiber probe, the foci of the 750-1000 nm and 1100-1450 nm inputs were axially chromatically shifted. The interference signals from the two spectral bands were measured with a Si camera-based spectrometer and an InGaAs camera-based spectrometer, respectively. We verified the feasibility of the design using a phantom composed of microparticles and swine small intestine tissue *ex vivo*. The results showed that a transverse resolution below 5 µm over 300 µm could be maintained, and that the extended DOF was 2 times larger than that of the single focus probe via the use of dual spectral band inputs and a chromatic focal shift.

OCIS codes: *(110.4500) Optical coherence tomography; (120.3180) Interferometry; (300.6300) Spectroscopy.*

http://dx.doi.org/10.1364/AO.99.099999

1. Introduction

Optical coherence tomography (OCT) [1,2] is a noninvasive imaging technique that enables cross-sectional imaging in biological tissues and materials, and it is used to diagnose a variety of human diseases. With the advent of supercontinuum light sources and depth of focus (DOF) extension techniques, the transverse resolution of desktop OCT devices has been improved from >10 µm to 1-3 µm, and this unprecedented spatial resolution enables the visualization of (sub)-cellular-level details [3-5]. However, the transverse resolution of current endoscopic OCT devices is still limited to 15-30 µm [6], which is mainly due to difficulties in incorporating DOF extension designs in the distal end of an OCT fiber optic probe.

Endoscopic OCT affords high-resolution three-dimensional (3D) in vivo visualization of internal luminal organs, and has emerged as a valuable tool for advancing our understanding of the histomorphology [7]. Continuued efforts have been excerted to improve the spatial resolution in order to obtain more detailed histopathological information [7-10]. The well-known trade-off between the lateral resolution and the depth of focus has been dealt with depth of focus extension through spherical and chromatic aberrations [11], pupil apodization [12], phase mask [13] and wavefront division multiplexing [14]. However, all of these previous attempts extend the depth of focus at the expense of coupling loss and sidelobe artifacts and consequently image quality and penetration depth.

The transverse resolution is mainly dependent on the numerical aperture (NA) of the effective objective lens. To achieve a high transverse resolution over an extended DOF, various approaches have been reported in the past decade. Generally, these methods can be classified into three categories: wavefront modification [14-17], phase or amplitude apodization [18-22], and digital refocusing [23-24]. The wavefront modification methods include multifocal methods and Bessel beam-involved DOF extension methods. These methods produce multiple focal regions or a focal line along the optical axis and maintaining a uniform transverse distribution over an extended DOF. However, such methods suffer from considerable signal loss, and Bessel beam methods produce pronounced side lobe artifacts [14-17]. Phase or amplitude apodization techniques also suffer from similar problems [18-22]. The digital refocusing approach has drawn great research interest because it requires minute hardware changes. Efforts related to interferometric synthetic microscopy (ISAM) [23] and synthesis aperture [24, 25] have been reported, however, the circumferential scanning required in endoscopic imaging settings is an obstacle that has not been overcome. Most of these solutions either suffer considerable signal loss or are not suitable for trans-endoscopic probes designed to assess luminal organs via natural orifices.

To address this technical barrier, we develop a chromatic dual-focus OCT fiber-optic probe to achieve a 2-fold DOF extension compared with that of a single focus probe with comparable transverse resolution.

2. Method

A. Chromatic dual-foci OCT system

A supercontinuum source (NKT, DK-3460, Birkerød, Denmark) was used to provide a spectral output from 750-1450 nm. We used a dichroic filter (DMSP950) and a notch filter (NF1064-44) (Thorlabs Inc., Newton, New Jersey, USA) to spectrally split the beam into a 750-950 nm beam (blue paths in Figure 1) and 1100-1450 nm beam (red). The short wavelength beam was focused by the achromatic lens L3 (f=15 mm, AC050-015-B, Thorlabs, USA) into fiber coupler FC1 (TW850R5F2, Thorlabs, USA) with a working spectral band of 750nm-1000nm, and the long wavelength beam was coupled into the fiber coupler FC2 (TW1300R5F2, Thorlabs, USA) with a working spectral band of 1100nm-1400nm through the achromatic lens L4 (f= 15mm, AC050-015-C, Thorlabs, USA). Both beams were guided to the probe. The backscattered interference signals conveyed on each wavelength section were guided back to the corresponding fiber couplers and spectrometers. Spectrometer 1 was composed of a 1200 line/mm grating (G1) (Wasatch Photonics 840nm, Munich, Germany), a camera lens (Nikon AF Nikkor 85mm f/1.8D), and a Si CCD camera (E2V,AViiVA EM4, Chelmsford, UK). Spectrometer 2 consisted of a 622 line/mm transmission grating (G2) (Ibsen Photonics NIR-622-901, Farum, Denmark), a camera lens (Nikon AF Nikkor 50mm f/1.8D), and an InGaAs CCD camera (Sensor Unlimited GL2048L, Princeton, NJ).

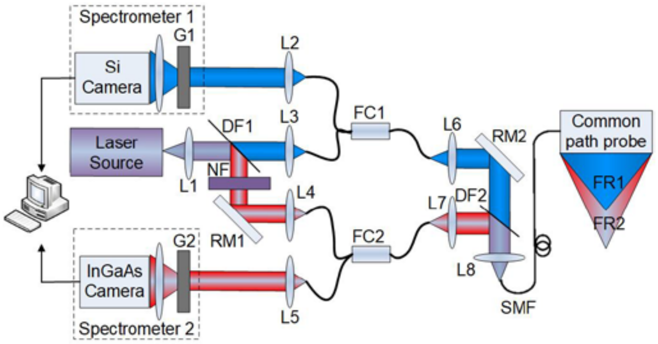

Fig. 1. Schematic of the chromatic dual-foci OCT system. L1-8, lenses with focal length f=10mm; FC1-2, fiber coupler; DF1-2, dichroic filter; NF, notch filter; RM1-2, reflective mirror; SMF, single mode fiber; G1-2, grating; FR1-2, focal region.

B. Common path probe

The common path probe used in the system was composed of a single mode fiber with fiber ferrule, a glass spacer (Edmund Optics, #54-087, Singapore), a GRIN lens (LFRL-200-023-50-810, Grintech, Germany), a beam splitter, and a reflective glass spacer. The fiber ferrule had a 2mm outer diameter and 126 μm inner diameter. An 8° angle was polished at the surface between the fiber ferrule and the BK7 spacer in case of fiber end reflection. The length of the BK7 spacer was polished to 3.5 mm, and the beam splitter was composed of a BK7 prism pair with gold surface plating and a 100 μm radius central obscure on the slope.

We numerically simulated the intensity distributions of the probe using scalar diffraction theory, and the results showed that this optical system generates two on-axis foci (Figure 2b). Figure 2c demonstrates the on-axis intensity distribution, which is designated by the dashed line in Figure 2b. As the two wave bands were guided into the same focal optics system, the foci of the two bands were separated due to a chromatic focal shift, which provided an individually extended DOF compared with a standard Gaussian beam. Figures 2b and 2c depict the simulated intensity distribution for the system with a fiber probe that consists of a single mode fiber (SMF), a spacer with a length of 3.5 mm, a GRIN lens with a NA of 0.5 at a wavelength of 810 nm, and a BK-7 prism with a leg length of 1.3 mm. As shown in the simulation results, two foci were introduced in the image space with a transverse resolution maintained below 5 μm over a 300 μm depth range.

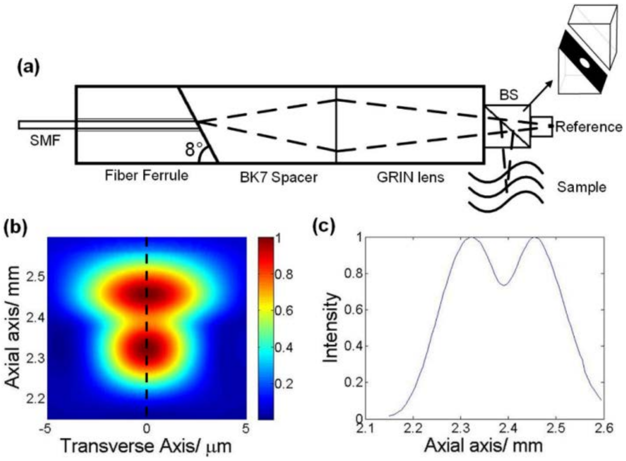

Fig. 2. (a) Schematic of the common path probe. SMF, single mode fiber; BS, beam splitter. (b) Simulated intensity distribution of the focus, color bar intensity is in linear scale with arbitrary units (a. u.). (c) Simulated on-axis intensity distribution.

C. System transverse resolution

The transverse resolution was measured from an image of the 1951 USAF Resolution Test Targets (R3L3S1P) (Thorlabs Inc., USA). For the intensity profiles of the bars on the resolution target, the system transverse resolution was shown to be 0.78 times the 10-90% edge width [26]. The two system transverse resolutions measurements were 2.1 μm and 3.3 μm at the two focal points of the short and long wavelength sections, respectively.

D. Imaging performance characterization

To characterize the optical performance of the system and fiber probe, we first constructed a phantom that consisted of 0.5% 2μm diameter polymer microbeads (Polysciences Inc, Cat# 64050, Warrington, UK) mixed with 1% agar (Vivantis, PC0701-500g, Malaysia). We also tested of the feasibility of our design on fresh full thickness swine small intestine tissue. The discarded swine digestive tracts were opened longitudinally and placed on the sample stage with the luminal surface up. Each specimen was flushed with PBS solution to remove the food debris and mucus. We used a motorized translation stage (Newport, M-VP-25XA, California, USA) to perform linear scanning for all the imaging experiments.

E. Intensity normalization

The chromatic dual-focus image was obtained by frame averaging the two spectral bands. Due to the dual-focus effect, the out-of-focus images in the short band frame affected the in-focus signal in the long band frame, and vice versa. Therefore, a digital intensity filter should be used to suppress the out-of-focus images for each of the frames. To acquire the intensity filter, a high-density microbeads phantom was sampled. After obtaining the phantom image, the intensity of every single microbeads image was quantitatively analyzed and the fitted curve was regarded as the intensity profile. The acquired intensity profile was used as the intensity filter multiplied by each A-line to obtain the in-focus images and suppress the out-of-focus images. Such a process was performed separately for the two spectral bands to enhance the in-focus signal.

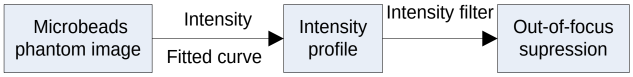

Fig. 3. Schematic of out-of-focus image suppression process.

Furthermore, to normalize the intensity of the two wavelength sections, the input power for the long wavelength section was increased to compensate for the signal-to-noise ratio (SNR) loss from the camera efficiency and the fiber core mismatch. The following steps were taken:

1. Obtain the in-focus A-line signal for each of the individual bands with a mirror placed at the sample arm.
2. Compare the signal power of the two acquired A-lines.
3. Adjust the input power of the two bands individually and repeat step 1 and 2 until the two spectral bands reach a comparable signal power.

Therefore, the illumination powers for the two wavelength sections were controlled separately. After testing the scattering phantom, the imaging SNR at the corresponding focal sites for both wavelength sections were optimized and measured at approximately 37 dB for the short wavelength section and 32 dB for the long wavelength section. The illumination powers of the two wavelength sections were measured separately at the sample arm of the common path probe once with only one wavelength section illumination, using power meter (PM100D) with a power sensor (S122C) (Thorlabs Inc.). The power was 7 mW at 830 nm for the short wavelength section and 20.6 mW at 1310 nm for the long wavelength section.

As the pixel resolutions of the two spectrometers were different and both CCDs share the same pixel number of 2048, the difference in bandwidth of the two wavelength sections caused a problem that the image depths of the two images were different. To match the two frames, the process was to place a glass slide at the sample and move the slide axially to obtain 20 frames. The image from the two spectrometers was realigned digitally based on the acquired frames

3. Result

A. Sensitivity

To evaluate the measured sensitivity, we analyzed the SNR in the case of an individual camera using the following formulas [27]:

$$S[dB] = 10 \times \log\left(\frac{N_{ref} \times \sum N_s}{N_{sh}^2 + N_{el}^2 + N_{RIN}^2}\right) \quad (1)$$

$$\frac{\sum N_s}{N_{ref}} = \frac{\sum P_s}{P_{ref}} \quad (2)$$

$$N_{RIN} = (f / \Delta v)^{1/2} N_{ref} \quad (3)$$

where N_{sh} is the number of shot noise electrons per pixel, N_{el} is the electrical noise of the photodetector per pixel, N_{RIN} is the relative intensity noise (RIN) per pixel, N_{ref} is the number of electrons per pixel generated by the reference arm light, $\sum N_s$ corresponds to the number of electrons over the entire array generated by the sample arm light returning from a 100% reflector without any attenuation, f denotes the line rate of the CCD, Δv denotes the FWHM spectral bandwidth of the reference light received by a single pixel, P_{ref} is the reflected reference power detected per pixel, and $\sum P_s$ denotes the sum of reflected power from the sample arm.

The system theoretical sensitivities were analyzed and are shown in Table 1. $\sum N_s$ was obtained by the returning power with the sample arm placing a mirror. Assuming a uniform spectral density, sensitivities of 93.9dB for the short wavelength section and 92.1dB for the long wavelength section were found. In our experiment to characterize the sensitivity of the system, we measured the SNR using a neutral density filter and a glass slide sample. The sensitivities for the two wavelength sections were measured separately.

Figure 4 shows the log power scale point spread functions (PSF). The two PSFs were obtained by placing the glass slide at the focal point of the two sections. To attenuate the sample power for sensitivity measurement, we used a partial reflector (-14dB) and a neutral density filter (-17.2 dB and -21.6dB at the long wavelength and short bands, respectively). The resulting sensitivities for the system were 90.52 dB at the short wavelength section and 87.43 dB at the long wavelength section. The cause of the difference between the theoretical and measured sensitivity was likely the spectral response non-uniformity of both cameras.

Table 1. Parameters for Sensitivity Analysis

	Short Wavelength Section (Si)	Long Wavelength Section (InGaAs)
Full Well Depth	312,500	2,100,000
$N_{RIN}=N_{el}$ (e^-)	137	872
F (Hz)	20480	20480
Δv	48.6 GHz	24.1 GHz
N_{ref} (e^-)	2.11×10^5	9.46×10^5
N_{sh} (e^-)	460	973
$\sum N_s$ (e^-)	2.94×10^9	4.31×10^9
Sensitivity (dB)	93.9	92.1

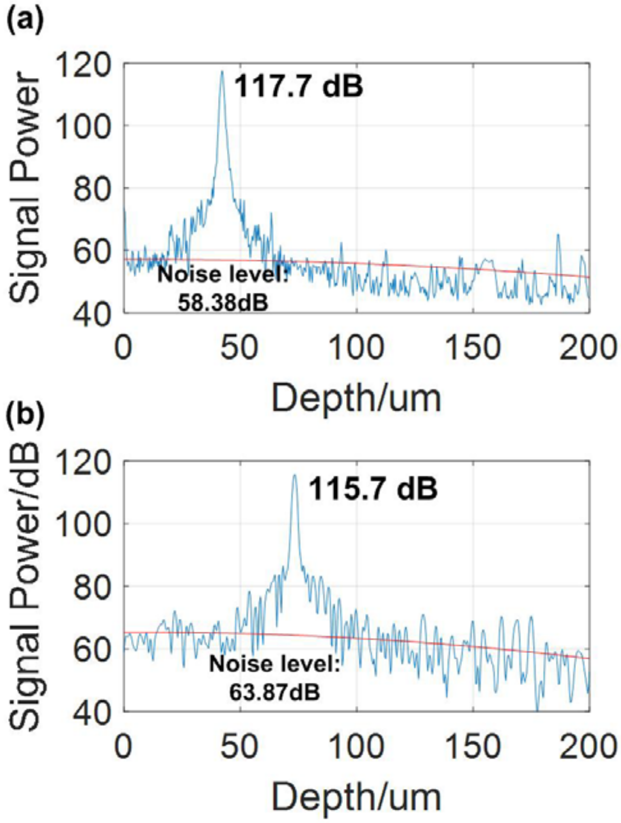

Fig. 4. Point spread function obtained with a glass slide sample and a neutral density filter. (a) At the focal point of the short wavelength section (total attenuation: -31.2 dB). (b) At the focal point of long wavelength section (total attenuation: -35.6 dB).

B. Axial resolution

The two axial resolutions of the corresponding spectral bands were measured on the PSFs obtained with a glass slide sample. Figure 5 shows that the axial resolutions for the two bands were 1.78 µm (short) and 2.3 µm (long), respectively. The theoretical axial resolutions were calculated using Eq (4).

$$l_c = \frac{2\ln 2}{\pi}\frac{\lambda_0^{\ 2}}{\Delta\lambda} \tag{4}$$

where λ_0 is the central wavelength and $\Delta\lambda$ denotes the bandwidth. The two spectral bands were 750-1000nm and 1100-1450nm. Therefore, the theoretical axial resolutions for the two bands were 1.59 µm and 2.04 µm. The difference between the theoretical and measured axial resolution resulted from the effect of chromatic focal shift within each spectral band. The results indicate that the influence of the chromatic focal shift on the image quality was comparably low.

C. Axial Intensity profile

We used a glass slide to characterize the axial intensity profiles of each focus of the two beams. The peaks of measured axial intensity profiles were in good agreement with our theoretical prediction in Fig. 2c using Zemax software (Fig. 6). The axial profile combined with beams of both bands matches perfectly with that of the simulation result (Fig. 6).

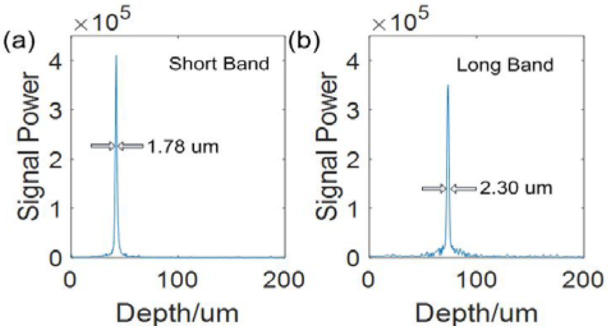

Fig. 5. Measured point spread functions. (a) The axial resolution of the short band was 1.78µm in air. (b) The axial resolution of the long band was 2.3µm in air.

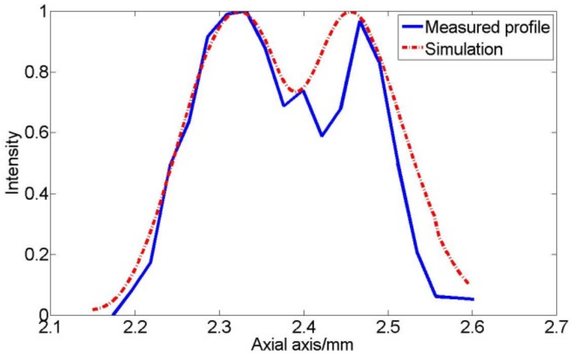

Fig. 6. Axial intensity profile compared with the simulation result.

D. Scattering phantom

Figure 7 shows the phantom images obtained by the dual-focus OCT system. Figures 7a and 7b are the phantom images obtained by each individual spectral band. By quantitatively analyzing the intensity of every single microbeads image, two intensity profiles were acquired for each of the bands. Before frame compounding, the two fitted curves demonstrated in Figure 7c and 7d were used as intensity filters. The two curves were multiplied by each A-line of the corresponding frame to obtain the in-focus images and suppress the out-of-focus images. Using the algorithm demonstrated in section 2.E, the chromatic dual-focus OCT images in Figure 7e were derived by frame averaging of the two in-focus image enhanced frames. The DOF extension effect was clearly resolved in Figure 7c, with bright and sharp microbeads images seen over an axial depth of over 300 µm, which doubled the DOF of the two images demonstrated in Figure 7a and 7b.

Figure 8 demonstrates the trend of width for the microbeads PSF. Figure 8a shows both wavelength sections. The width of the PSF increased dramatically when the images were out of the focal site. However, when chromatic dual-focus technology was implemented as shown in Figure 8b, the sharp profiles maintained a distance that was twofold greater than that of the single focus system.

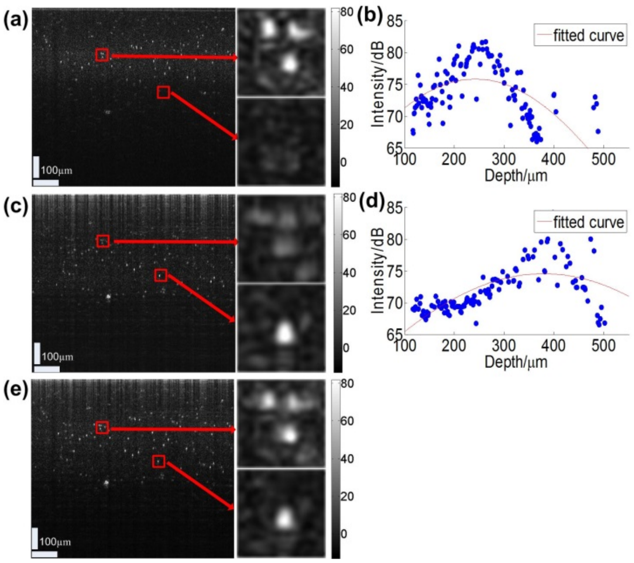

Fig. 7. Image of microbeads phantom. (a) The image acquired using the short wavelength band. Insert: magnified area of 20×20 μm. (b) Axial intensity profile of the short band. (c) The image acquired using the long wavelength band. Insert: magnified area of 20×20 μm. (d) Axial intensity profile of the long band. (e) Chromatic dual-focus OCT image. Inserts: magnified area of 20×20 μm.

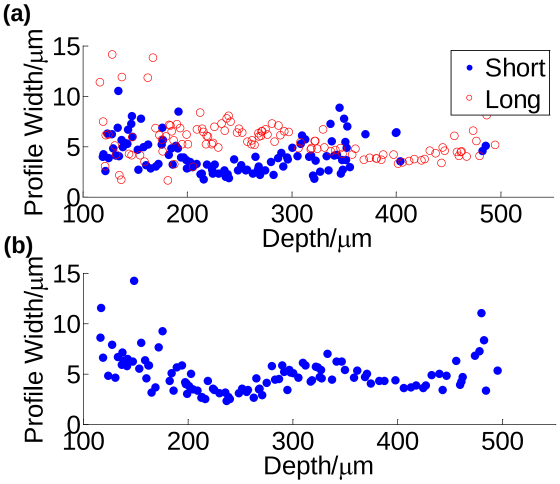

Fig. 8. Trend of width for the micro beads PSF. (a) Two wavelength sections. (d) Chromatic dual-focus design.

E. Swine small intestine

Specimens of swine small intestine were used to conduct OCT imaging ex vivo. The cross- sectional images of the specimens are presented in Figure 9.

As shown in Figure 9a, the crypt lumens to the upper part of the tissue were clearly resolved with good contrast relative to the epithelium in the short wavelength section image. However, sub-cellular level structures in the deeper part as shown by the arrows in the figure did not provide clear information due to out-of-focus artifacts. However, Figure 9b depicts the crypt lumen and goblet cells in the deeper part, and the sharp bright crypt lumen images in the upper part are sacrificed. The single focus system with only one wavelength section illumination has a limited DOF so that only part of the small intestine epithelium information can be resolved clearly on the two corresponding images. The two previous images were combined, and a chromatic dual-focus OCT image is shown in Figure 9c. With clear information of the crypt lumen and goblet cells resolved in the entire epithelium, the DOF extension effect was clearly verified.

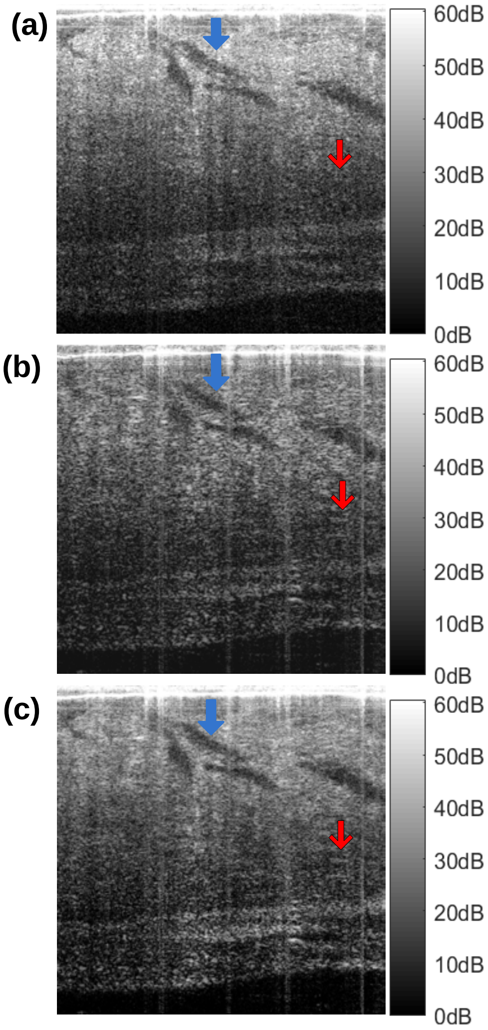

Fig. 9. *Ex vivo* images of swine small intestine cover an area of 512×902 μm (Lateral × depth). (a) The image acquired using the short wavelength band. (b) The image acquired using the long wavelength band.. (c) Chromatic dual-focus image.

4. Discussions

A. Multi-foci techniques

Producing multiple foci axially is a straightforward approach to the DOF limitation problem, and a few multifocal designs have been reported [12-14]. Although promising results have been achieved, existing multifocal designs are limited by either system complexity at the distal end of fiber-optic probes [12,13] or signal loss [14]. The proposed design takes advantage of the chromatic focal shift to produce two foci using the same fiber pinhole so that a standard distal end optics probe can be used via the application of a commercially available GRIN lens, thus, the proposed probe is easy to fabricate and more energy efficient. However, the capability of the proposed DOF extension technique is limited by both the available spectral bandwidth of the light source and the biological window.

B. Impact of apodization

The optical distal end in the proposed system was a common path probe. With the 100 µm radius central obscuration at the sample arm to perform as a beam splitter, apodization was introduced to the sample beam. Unlike other DOF extension technologies which rely on the apodized beam to extend the DOF [4,10], the lower level apodization caused by the relatively small central obscuration limited the signal loss and the sidelobe problems in our design. We conducted Zemax simulation and found the beam size at the plane of the obscuration was 1.02mm (FWHM). The obscuration caused a -13dB sidelobe level and a 0.68dB signal loss. Comparing to the existing DOF extension technologies, which suffer -11dB sidelobe level [4] and 1.5dB signal loss [10], the impact of apodization in our design is relatively small.

C. Trade-off between chromatic focal shift and spatial resolution

A spectral gap was observed between the detected spectra of the two spectrometers. As a result, both foci tended to defocus in an axial range between two foci. Since we aimed to achieve a diffraction-limited lateral resolution of 3 µm for both foci, the corresponding DOFs are 120 µm and 150 µm for the shorter band and longer band, respectively. To construct a DOF continuum, we chose GRIN with a diameter of 2 mm and length of 3.5 mm, so that the focal shift between the center wavelengths of the two spectral bands was approximately 150 µm. The spectral gap between the detected spectra may be filled by using line scan imaging sensors with an improved response of approximately 950 nm, thus, a spectral supercontinuum is achieved. In this case, a simple trade-off was observed between the DOF extension and axial resolution.

In our current probe design, the lateral resolution is depth dependent because the mode field diameter of the single mode fiber was wavelength dependent (from 780 nm to 970 nm). This issue may be solved by using a fiber with a wavelength independent mode field diameter, such as an endlessly single mode photonics crystal fiber.

D. Sensitivity considerations

The system sensitivities were 90.52 dB and 87.43 dB for the two wavelength sections. However, the sensitivity can be further improved, as the system sensitivities were not optimized due to fabrication constraints on the common path probe. Eqs. (1) and (2) can be used to derive the following:

$$S[dB] = 10 \times \log\left(\frac{\sum P_s}{P_{ref}} \times \frac{N_{ref}^2}{N_{sh}^2 + N_{el}^2 + N_{RIN}^2}\right) \qquad \textbf{(5)}$$

Eq. (5) shows that the system sensitivity should be proportional to the sample power. For desktop probes or non-common path optics probes, as the reference arm was not implemented on the optics probe, it was adjustable. The reference power could be maintained at an optimized level while increasing the sample power. However, for the fabricated common path probe, the ratio between the sample power and reference power became a constant, which was related to the size of the window on the beam splitter and the reflectance of the reference glass rod. As in our probe, the ratio $\sum Ps/Pref$ for short and long wavelength sections were 1.39×10^4 and 4.56×10^3, respectively. Furthermore, the optimized ratios were examined using a conventional desktop probe instead of an optics common path probe. The ratios were up to 1.11×10^5 and 3.94×10^4. In other words, the system sensitivity of 9 dB (9.02 dB and 9.36 dB for short and long wavelength sections) was reduced due to the fabrication constraint of the common path probe. With the current fabrication technique, we could not precisely control the window size and the reflectance, which increased the difficulty of optimizing the sensitivity. Furthermore, to reach a sufficient sensitivity for the proposed system, our power density was set at a high level and it was higher than the ANSI laser safety limit for exposure to skin. However, all experiments in the paper were performed ex-vivo and clear damage to the tissue was not observed. We have also conducted the histology examination to test the swine small intestine exposed under the system power density, the result shows that the proposed power density cause no damage to the tissue. Various of reasons, such as the mucus on the surface, difference in moisture content, and lacking of melanin, makes inner organ tissue especially GI tract tissue better at thermal dissipation than skin, thus the inner organ tissue is more resistant to exposure.

To make further improvements, a reflectance adjustable reference glass rod was needed. Efforts will also be made to include a smaller central obscuration to increase the power ratio between the sample and reference. Meanwhile, in future *in-vivo* experiments, study should be made on the thermal effect of GI tract to figure out the laser safety limit for exposure for inner organ tissue, system sensitivity and the frame rate should be adjusted to ensure that the system complies with the safety limit.

5. Conclusion

In conclusion, we have established a chromatic dual-focus technique to overcome the DOF limitation in high-resolution endoscopic OCT. The proposed method can provide diffraction-limited lateral resolution over a 2-fold extended DOF at the expense of a 2-fold increase in optical exposure and additional system complexity and costs. A practical application for the dual-focus device is to observe intraepithelial neoplasia in esophagus. The hyperplastic or dysplastic epithelium is normally thicker than the normal ones. To visualize epithelial rete pegs that may extend hundreds of micro-meters deep into stroma, the focus of the longer wavelength can be used to detect the morphology of rete pegs and possible infiltration of epithelial cancer cells into the lamina propria. The proposed method is superior to the existing DOF extension technologies in three aspects. First, a chromatic dual-focus design can be achieved with commonly used fiber-optic OCT probes; therefore, it can be readily used for various applications. Second, the proposed method experiences limited signal loss or sidelobe problems. Finally, our method can be used in combination with other technologies, such as wavefront engineering techniques and digital refocusing, to further improve the focusing performance.

Funding Information. This research was supported by National Research Foundation Singapore (NRF-CRP13-2014-05); National Natural Science Foundation of China (61705184); Ministry of Education Singapore (MOE2013-T2-2-107); National Medical Research Council Singapore (NMRC/CBRG/0036/2013); NTU-AIT-MUV program in advanced biomedical imaging (NAM/15005)

References

1. D. Huang, E. A. Swanson, C. P. Lin, J. S. Schuman, W. G. Stinson, W. Chang, M. R. Hee, T. Flotte, K. Gregory, C. A. Puliafito, and a. et, "Optical coherence tomography," Science **254**, 1178-1181 (1991).
2. G. J. Tearney, M. E. Brezinski, B. E. Bouma, S. A. Boppart, C. Pitris, J. F. Southern, and J. G. Fujimoto, "In vivo endoscopic optical biopsy with optical coherence tomography," Science **276**, 2037-2039 (1997).
3. R. A. Leitgeb, W. Drexler, A. Unterhuber, B. Hermann, T. Bajraszewski, T. Le, A. Stingl, and A.F. Fercher, "Ultrahigh resolution Fourier domain optical coherence tomography," Optics Express **12**(10), 2156-2165 (2004).
4. L. Liu, N Chen, and C.J.R Sheppard, "Double-reflection polygon mirror for high-speed optical coherence microscopy," Optics letters, **32**(24), 3528-3530 (2007).
5. X. Yu, Y. Luo, X. Liu, S. Chen, X. Wang, S. Chen, and L.Liu, "Toward High-Speed Imaging of Cellular Structures in Rat Colon Using Micro-optical Coherence Tomography," IEEE Photonics Journal **8**(4), 1-8 (2016).
6. M. E. Brezinski, G. J. Tearney, B. E. Bouma, S. A. Boppart, M. R. Hee, E. A. Swanson, J. F. Southern, and J. G. Fujimoto, "Imaging of coronary artery microstructure (in vitro) with optical coherence tomography," The American journal of cardiology **77**(1), 92-93 (1996).
7. W. Yuan, R. Brown, W. Mitzner, L. Yarmus, and X. Li. "Super-achromatic monolithic microprobe for ultrahigh-resolution endoscopic optical coherence tomography at 800 nm," Nature communications, **8**(1), 1531 (2017).
8. S. A. Boppart, B. E. Bouma, C. Pitris, J. F. Southern, M. E. Brezinski, and J. G. Fujimoto. "In vivo cellular optical coherence tomography imaging," Nature medicine, **4**(7), 861-865 (1998).
9. Y. Luo, D. Cui, X. Yu, E. Bo, X. Wang, N. Wang, S. B. Cilwyn, S. Chen, X. Liu, Q. Xiong, Si Chen, S. Chen, and L. Liu, "Endomicroscopic optical coherence tomography for cellular resolution imaging of gastrointestinal tracts," Journal of biophotonics, **11**(4), e201700141 (2018).
10. B. Yin, C. Hyun, J. A. Gardecki, and G. J. Tearney, "Extended depth of focus for coherence-based cellular imaging," Optica, **4**(8), 959-965 (2017).
11. H. Schulz-Hildebrandt, M. Pieper, C. Stehmar, M. Ahrens, C. Idel, B. Wollenberg, K. Peter, and G. Hüttmann, "Novel endoscope with increased depth of field for imaging human nasal tissue by microscopic optical coherence tomography," Biomedical Optics Express, **9**(2), 636-647 (2018).
12. D. Cui, K. K. Chu, B. Yin, T. N. Ford, C. Hyun, H. M. Leung, J. A. Gardecki, G. M. Solomon, S. E. Birket, L. Liu, S. M. Rowe, and G. J. Tearney, "Flexible, high-resolution micro-optical coherence tomography endobronchial probe toward in vivo imaging of cilia," Optics letters, 42(4), 867-870 (2017).
13. D. Lorenser, X. Yang, and D. D. Sampson, "Ultrathin fiber probes with extended depth of focus for optical coherence tomography," Optics letters, **37**(10), 1616-1618 (2012).
14. B. Yin, K. K. Chu, C. P. Liang, K. Singh, R. Reddy, and G. J. Tearney, "μOCT imaging using depth of focus extension by self-imaging wavefront division in a common-path fiber optic probe," Optics express, **24**(5), 5555-5564 (2016).
15. R. Leitgeb, M. Villiger, A. Bachmann, L. Steinmann, and T. Lasser, "Extended focus depth for Fourier domain optical coherence microscopy," Optics letters **31**, 2450-2452 (2006).
16. V. X. Yang, N. Munce, J. Pekar, M. L.Gordon, S. Lo, N. E. Marcon, and I. A. Vitkin, "Micromachined array tip for multifocus fiber-based optical coherence tomography," Optics letters **29**(15), 1754-1756 (2004).
17. W. Bao, Z. Ding, J. Qiu, Y. Shen, P. Li, and Z. Chen, "Quasi-needle-like focus synthesized by optical coherence tomography," Optics letters **42**(7), 1385-1388 (2017).
18. L. Liu, F. Diaz, L. Wang, B. Loiseaux, J.-P. Huignard, C. Sheppard, and N. Chen, "Superresolution along extended depth of focus with binary-phase filters for the Gaussian beam," JOSA A **25**, 2095-2101 (2008).
19. D. Lorenser, X. Yang, and D. D. Sampson, "Ultrathin fiber probes with extended depth of focus for optical coherence tomography," Optics letters **37**, 1616-1618 (2012).
20. Y. Xu, J. Singh, C. J. Sheppard, and N. Chen, "Ultra long high resolution beam by multi-zone rotationally symmetrical complex pupil filter," Optics express **15**, 6409-6413 (2007).
21. L. Liu, J. A. Gardecki, S. K. Nadkarni, J. D. Toussaint, Y. Yagi, B. E. Bouma, and G. J. Tearney, "Imaging the subcellular structure of human coronary atherosclerosis using micro-optical coherence tomography," Nature medicine **17**, 1010-1014 (2011).
22. X. Yu, X. Liu, J. Gu, D. Cui, J. Wu, and L. Liu, "Depth extension and sidelobe suppression in optical coherence tomography using pupil filters," Optics express **22**, 26956-26966 (2014).
23. T. S. Ralston, D. L. Marks, P. S. Carney, and S. A. Boppart, "Interferometric synthetic aperture microscopy," Nature Physics **3**, 129-134 (2007).
24. J. Mo, M. de Groot, and J. F. de Boer, "Focus-extension by depth-encoded synthetic aperture in Optical Coherence Tomography," Optics express **21**, 10048-10061 (2013).
25. E. Bo, Y. Luo, S. Chen, X. Liu, N. Wang, X. Ge, X. Wang, S. Chen, S. Chen, J. Li, and L. Liu, "Depth-of-focus extension in optical coherence tomography via multiple aperture synthesis," Optica **4**(7), 701-706 (2017).
26. M. Rajadhyaksha, R. R. Anderson, and R. H. Webb, "Video-rate confocal scanning laser microscope for imaging human tissues in vivo," Applied optics **38**(10), 2105-2115 (1999).
27. S. H. Yun, G. J. Tearney, B. E. Bouma, B. H. Park, and J. F. de Boer, "High-speed spectral-domain optical coherence tomography at 1.3 μm wavelength," Optics express, **11**(26) 3598-3604 (2003).